Available online at www.sciencedirect.com
ScienceDirect
International Journal of Heat and Mass Transfer 50 (2007) 5099–5107
International Journal of HEAT and MASS TRANSFER
www.elsevier.com/locate/ijhmt

Thermal conduction induced by electron-beam

Basil T. Wong [a], M. Pinar Mengüç [a,*], R. Ryan Vallance [b]

[a] Department of Mechanical Engineering, University of Kentucky, Lexington, KY 40506-0108, USA
[b] Mechanical and Aerospace Engineering, The George Washington University, Washington, DC 20052, USA

Received 12 December 2006; received in revised form 9 May 2007
Available online 11 September 2007

Abstract

The electron-energy deposition profile within the workpiece, induced by a perpendicularly impinging electron-beam, is obtained by solving the electron-beam transport equation via a Monte Carlo approach. The profile serves as the external electron generation in the two-temperature model. The beam is assumed to be a continuous source (not pulsed), and the energy exchange between the electron-beam and the target workpiece occurs at a time scale much shorter than the characteristic time of thermal conduction by electrons and phonons inside the workpiece. A series of numerical results explain the details of the heating phenomena at the nanoscale using an electron-beam.

Keywords: Nanomachining; Two-temperature model; Electron-beam propagation; Monte Carlo method; Sublimation; Electron–phonon coupling

1. Introduction

Material processing with high-power lasers has been used extensively in numerous industrial applications to produce structures or patterns on material surfaces, including micrometer size structures. Resolutions of these structures depend greatly on the incident spatial distribution of the laser beam. Due to photon diffraction, a laser has a maximum focus of one-forth to one-fifth of its wavelength. The typical wavelength of a laser used in material processing is on the order of hundreds of nanometers. Therefore it is not possible to create features of a few nanometers using conventional laser machining approaches, which are usually based on far-field optical arrangements. Alternatives, such as X- or gamma-rays may be used for nanoscale machining, yet, the cost required for such processes is high. Another approach for achieving nanomachining would be to utilize energized electrons emitted from a nanoscale probe, such as a carbon nanotube (CNT). The electrons would bombard the solid target and create localized structural changes. Electrons have wavelengths much smaller than those of photons, which negates diffraction effects until a size of less than a nanometer is reached. Focusing the electron-beam to a few nanometers can be achieved using electrostatic or electromagnetic lenses.

Recently, Vallance et al. [1] proposed a possible nanomachining tool using an electron-beam produced by a sharp tip, such as a carbon nanotube. A schematic of the proposed physical system is depicted in Fig. 1. The system is mainly comprised of an anode and a cathode operating in a ultra-high vacuum environment. The anode is referred to as the ‘workpiece’ since machining will be performed on it; the cathode is the machining tool, or the nanoprobe. Voltage applied between the anode and the cathode causes energized electrons to flow from the cathode to the anode. These electrons bombard the target workpiece, transferring a considerable amount of kinetic energy to the workpiece, which could subsequently cause material removal by evaporation.

While the concept has significant potential, the underlying heat transfer mechanism is not well-understood. Understanding the details of heat transfer is important

---

* Corresponding author. Tel.: +1 859 257 6336x80658; fax: +1 859 257 3304.
E-mail address: menguc@engr.uky.edu (M.P. Mengüç).

0017-9310/$ - see front matter © 2007 Elsevier Ltd. All rights reserved.
doi:10.1016/j.ijheatmasstransfer.2007.07.028

Nomenclature

c	speed of light
C	heat capacity
E	electron-energy
f	a scattering factor
g	a scattering factor
G	electron–phonon coupling constant
k	electron wave number
k_B	Boltzmann's constant
k_e	electronic thermal conductivity
l	mean free path
m	mass of electron
P	Legendre polynomial
R	cumulative probability distribution function
Ran	random number
S	distance of interaction
S_T	external heat generation term
T	temperature

Greek symbols

δ	Dirac phase shifts
σ	scattering cross section
$\hbar$	Planck's constant

Subscripts

e	electrons
eff	effective
el	elastic
F	Fermi
inel	inelastic
ph	phonons

for predicting the amount of energy required from the electron-beam to remove nanoscale amounts of material from the target workpiece. In a previous study, we considered a similar problem; electron-beam propagation in the workpiece was analyzed with a Monte Carlo (MC) simulation, and the Fourier law was used to model heat conduction [2]. The MC simulation provided the electron-energy deposition profile, which served as the heat source term in the heat diffusion equation. The MC simulation procedures were based on the continuous slow-down approach (CSDA), which treated the energy loss of electrons (from the electron-beam) inside the workpiece as continuous phenomena along the line of propagation.

Fourier's law does not account for the electron-temperature within the workpiece. To remedy this, the two-temperature model (TTM) that distinguishes between the electron-temperature and the phonon-temperature is used here. Also, an alternative MC simulation, which includes the generation of secondary electron inside the workpiece, replaces the CSDA in simulating the electron-beam propagation.

2. Problem description

A single electron-beam impinging perpendicular to a 3-D region of the target workpiece is considered. A simple schematic of the problem is given in Fig. 1b. When the electron-beam hits the workpiece, "hot" electrons spread inside the workpiece, as depicted by the dark region in the figure. When these electrons transfer their energy to the workpiece, a high temperature region is created (i.e. the red shaded region in the figure). The target workpiece is assumed to have a perfect lattice structure. The electron-beam is assumed to have a Gaussian spatial distribution when incident on the surface of the workpiece. The workpiece has finite dimensions in all three directions. The entire system is assumed to be inside a vacuum chamber.

In traditional Fourier's law, there is no temperature difference between electrons and phonons because there is no differentiation between the two energy carriers. When the energized electrons from the electron-beam penetrate the workpiece, kinetic energy from these electrons is assumed to transfer simultaneously to both electrons and phonons. In this work, electrons and phonons can co-exist at different temperatures. When electrons from the electron-beam enter the target, energy is first transferred to electrons inside the workpiece, elevating the electron-temperature. Subsequently, the phonon-temperature increases through collisions between electrons and phonons inside the workpiece.

Material ablation is not considered in this work. The mean ionization energy of gold is 790 eV [3]. Our simulation temperature is less than 1000 K. Converting the electron-temperature to energy using the Boltzmann constant, we find $k_B T = 8.6 \times 10^{-5}$ eV/K $\times$ 1000 K $= 0.086$ eV, which is much smaller than the mean ionization energy of gold. In addition, the initial kinetic energy of our electron-beam is set to 500 eV in the simulation. Therefore, ionization of gold should not be of concern.

3. Computational methods

To solve this problem numerically, the electron-energy deposition profile is first determined from the MC simulation. This profile is then treated as the heat source in the electron-temperature equation, which is coupled with the phonon-temperature equation. Both are solved simultaneously in order to predict the temperature distributions.

3.1. Computational grid

The workpiece is assumed to be gold, and the electron-beam bombards the target from above. To account for electron-beam transport and heat conduction for the

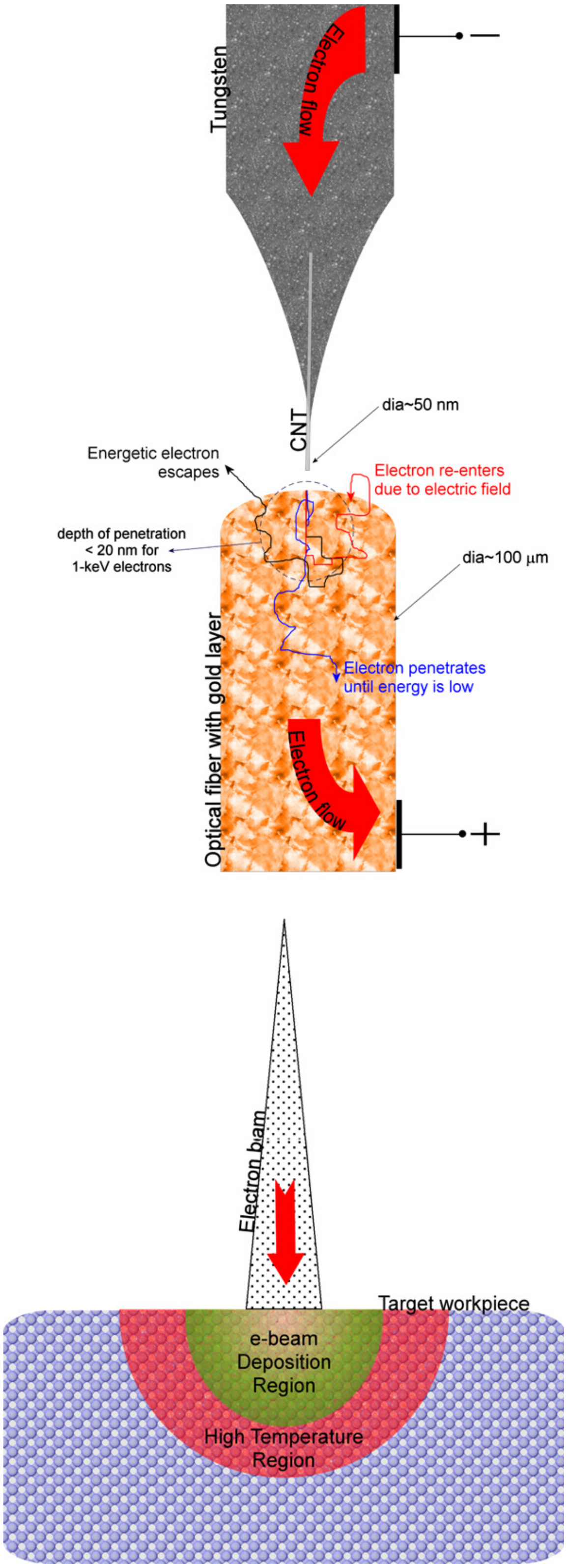

Fig. 1. (a) Schematic of the proposed machining process using electron field emission from a nano-probe. Note that the schematic is not drawn to scale. The actual size of the carbon nanotube (CNT) is about 50 nm in diameter while the optical fiber has a diameter of hundreds of microns. The fiber is considered to be infinite compared to the nanotube. (b) The simple schematic of the workpiece as it is exposed to the electron-beam heating.

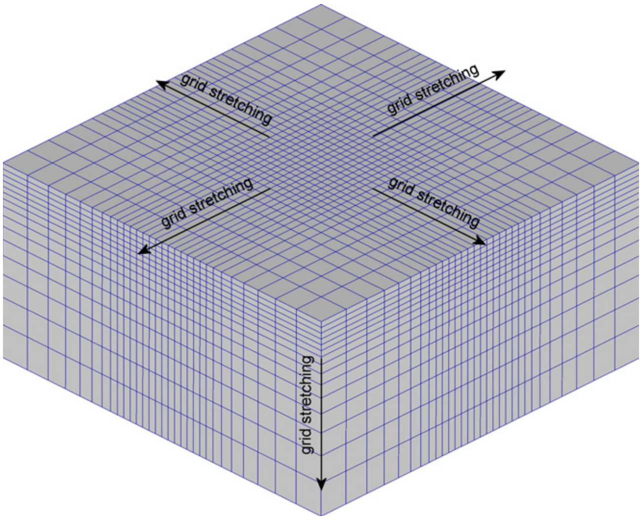

Fig. 2. A sample of the structure of the grid. Note that they are not the actual grid spacings, as they have been adjusted for display clarity.

relatively large dimensions of the workpiece, the grid away from the origin is stretched to minimize the number of computational elements. ‘Relatively’ describes the comparison between the spatial energy spread of the incident electron-beam and the overall dimension of the geometry. The origin is located at the top center of the geometry, where the electron-beam first hits. The structure of the computational grid is depicted in Fig. 2. The grid spacing in all directions is uniform at the center of the cross-sectional area, as well as near the top of the domain. The MC simulation for the electron-beam transport is performed within the uniform grid. The uniform grid region is chosen such that the electron-energy deposition profile is well-confined within it.

3.2. Electron-beam monte carlo simulation

In our previous publications [2,4], a MC simulation was adapted from the CSDA. The basics of this method are similar to a typical Monte Carlo simulation in which ensembles are launched and forced to propagate according to certain cumulative probability distribution functions (CPDF) derived from the governing scattering phenomena. In this method, the propagating ensembles of electrons are assumed to lose kinetic energy along the path of propagation. The amount of energy lost is generally proportional to the distance traveled. This amount is computed using the stopping power of electrons (i.e. the amount of energy lost per unit distance, as suggested in Refs. [3,5]), and equally divided along the path. The exponential decaying of electron-energy is embedded in the simulation through the CPDF of the distance of interaction. This approach is common when analyzing electron microscopy [3,5].

A different version of MC simulation, called discrete inelastic scattering (DIS), is employed in this work. The major difference between this method and the CSDA is the treatment of the inelastic scattering events, while the procedures of simulating elastic scattering remain unaltered. As the name implies, the DIS method treats the inelastic scatterings as point scattering events; hence, an inelastic scattering mean free path is employed. Ding and Shimizu [6] outlined this method in an orderly fashion, and the procedures given in the reference are followed closely in this analysis.

The simulation procedures of the DIS method are very similar to that of the CSDA or any typical MC simulation in particle-beam transport [7]. The simulation starts by sampling the launching location of the ensemble. The ensemble is then launched with its known initial energy, and later scattered continuously by the workpiece until its energy becomes low. The scattering distance includes both mean free paths of the elastic and inelastic scattering events. When this method is employed, the CPDF of both elastic and inelastic scatterings is incorporated into a single equation, which is given as

$$R(S_{\mathrm{eff}}) = \exp(-S_{\mathrm{eff}}/l_{\mathrm{eff}}), \tag{1}$$

where l_{eff} is the effective mean free path computed from both elastic and inelastic mean free path (i.e. l_{el} and l_{inel}, respectively)

$$l_{\mathrm{eff}}^{-1} = l_{\mathrm{el}}^{-1} + l_{\mathrm{inel}}^{-1}. \tag{2}$$

Therefore, the distance of interaction is given as

$$S_{\mathrm{eff}} = -l_{\mathrm{eff}} \ln(\mathrm{Ran}_{\mathrm{S}}), \tag{3}$$

where $\mathrm{Ran}_{\mathrm{S}}$ is a random number. This is the distance a particle travels before an elastic or inelastic scattering event occurs. Upon interaction, another random number, $\mathrm{Ran}_{\mathrm{I}}$, decides whether the event is elastic or inelastic. The electron is scattered elastically if $\mathrm{Ran}_{\mathrm{I}} < l_{\mathrm{el}}^{-1}/l_{\mathrm{eff}}^{-1}$ and inelastically if $\mathrm{Ran}_{\mathrm{I}} \geqslant l_{\mathrm{el}}^{-1}/l_{\mathrm{eff}}^{-1}$. The amount of kinetic energy loss needs to be determined from the probability of inelastic scattering per unit length and energy change (i.e. $\mathrm{d}l_{\mathrm{inel}}^{-1}/\mathrm{d}(\Delta E')$). The CPDF for the amount of energy change is then expressed using this probability as

$$R = \int_0^{\Delta E} \frac{\mathrm{d}l_{\mathrm{inel}}^{-1}}{\mathrm{d}(\Delta E')}\mathrm{d}(\Delta E') \bigg/ \int_0^{E-E_{\mathrm{F}}} \frac{\mathrm{d}l_{\mathrm{inel}}^{-1}}{\mathrm{d}(\Delta E')}\mathrm{d}(\Delta E'). \tag{4}$$

In the limits of the integration, the possible amount of kinetic energy loss of electrons ranges from none to the difference between the current kinetic energy E and the Fermi energy E_{F} of the target material. After that, the scattering direction is determined according to the type of scattering event. The CPDF of the elastic scattering is derived from the Mott scattering cross-section, while that of the inelastic scattering requires the use of dielectric theory.

The Mott elastic differential scattering cross section for an electron beam is typically given in the form of Eq. (5) [5,15–17].

$$\frac{\mathrm{d}\sigma_{\mathrm{e}}^{\mathrm{el}}(E)}{\mathrm{d}\Omega} = |f|^2 + |g|^2. \tag{5}$$

The scattering factors f and g are functions of a scattering polar angle Θ. The scattering factors are expressed in the following forms [15–17]:

$$f(\Theta, k) = \frac{1}{2ik}\sum_{l=0}^{\infty}\left\{(l+1)[\mathrm{e}^{2\mathrm{i}\delta_{-l-1}} - 1] + l[\mathrm{e}^{2i\delta_l} - 1]\right\}P_{\mathrm{l}}(\cos\Theta), \tag{6}$$

$$g(\Theta, k) = \frac{1}{2\mathrm{i}k}\sum_{l=1}^{\infty}[-\mathrm{e}^{2\mathrm{i}\delta_{-l-1}} + \mathrm{e}^{2\mathrm{i}\delta_l}]P_l^*(\cos\Theta). \tag{7}$$

Here, P_{l}'s and P_{l}^*'s are the ordinary Legendre polynomials and the associated Legendre polynomials, respectively, and δ_{l}'s are the Dirac phase shifts. In the above expressions, k represents the wave number of the electron with energy E. They are related according to

$$k^2 = \frac{(E^2 - m^2c^4)}{\hbar^2c^2}, \tag{8}$$

where $\hbar$ is angular Planck's constant, c is the speed of light, and m is the mass of electrons. The phase shifts are determined from the Dirac equation, which describes the relativistic behavior of an electron, including its spin, the magnetic moment of the electron, and the spin-orbit coupling.

The dielectric formulation directly employs the energy loss function derived from the experimental optical data and generates the differential inelastic scattering cross section accordingly. Since the energy loss function is a measure of responses of electrons and atoms in a medium as a whole (when exposed to an external disturbance), it is typically more accurate compared to other independent formulations, especially when the electron-energy is low. In this way, the inner-shell ionizations (if any) and the outer-shell excitations cannot be distinguished clearly. Nevertheless, it is a better approach for determining the inelastic scattering properties of electrons at low energy, considering that the inelastic electron scatterings are not currently well-understood at the low electron-energy regime. Details on these procedures are quite elaborate, and are therefore not presented here. Interested readers are referred to the paper by Ding and Shimizu [6].

These simulations account for the generation of secondary electrons. Whenever an inelastic scattering event occurs, a secondary electron will be "born" if the amount of energy transferred to the electron inside the material is greater than the Fermi energy level. The propagation of these secondary electrons is treated following the same fashion as the primary electrons (i.e. electrons originating from the electron-beam). The electrons undergo a series of elastic and inelastic scattering events, and additional secondary electrons may emerge due to energy transfer from these electrons. This causes a cascade effect, and it prolongs the simulation due to these additional electron interactions. Overall, all the electron ensembles propagate until they either exit the medium or their energies fall below that of the surface barrier. Further details of these equations and simulation procedures are available elsewhere [4,6].

The electron-energy deposition distribution within the workpiece is obtained after all of the propagations of electron ensembles are terminated and recorded, in their respective locations. In the simulation, the energies of the electron ensembles are tracked continuously, maintaining energy conservation at all times. After the MC simulation is completed, the electron-energy distribution within the material is determined per unit of energy originally emitted from the cathode. Each computational element is normalized by the total amount of electron-energy supplied from the electron-beam and its elemental volume. Therefore, in order to use the electron-energy distribution in the two-temperature model, one needs to provide the power of the electron-beam or the current of the beam, because the voltage (which determines the initial kinetic energy of the electrons emerging from the nanoprobe) is fixed when the MC simulation starts.

3.3. Two-temperature model

Interactions between external heating sources, such as the photon- and electron-beams, and the target workpiece involve heating of the electron gas inside the target workpiece, which causes the electron-temperature to elevate substantially compared to the lattice temperature. One way to model this phenomenon is to separate temperature into two distinct components, namely the electron-temperature and the phonon-temperature. Such a model is usually referred to as the two-temperature model (TTM) [8]. The TTM is expressed in two equations. The first is the electron-energy conservation equation, and the second is the phonon-energy conservation equation.

$$C_{\mathrm{e}}\frac{\partial T_{\mathrm{e}}}{\partial t} = -\nabla\cdot(k_{\mathrm{e}}\nabla T_{\mathrm{e}}) - G_{\mathrm{e\text{-}ph}}(T_{\mathrm{e}} - T_{\mathrm{ph}}) + S_{\mathrm{T}}, \tag{9}$$

$$C_{\mathrm{ph}}\frac{\partial T_{\mathrm{ph}}}{\partial t} = -G_{\mathrm{e\text{-}ph}}(T_{\mathrm{ph}} - T_{\mathrm{e}}). \tag{10}$$

The subscripts ‘e’ and ‘ph’ denote that of electrons and phonons, respectively. The C’s are the heat capacities of the energy carriers, and k_{e} is the thermal conductivity of electrons. The electron–phonon coupling constant is denoted as $G_{\mathrm{e\text{-}ph}}$. With an electron-beam impinging on the workpiece, $G_{\mathrm{e\text{-}ph}}$ might change according to the increase in the local electron density. It requires an in-depth investigation and supporting experimental data to access this effect, which is beyond the scope of the present work. Therefore, we assume that $G_{\mathrm{e\text{-}ph}}$ remains constant and follows the value given in the literature (see Table 1).

In MC simulations, we assume energetic electrons lose energies along the path of propagation due to inelastic scattering events, which mostly involve energy exchanges between electrons from the beam and the electrons within the material. Atoms are solely responsible for deflecting the penetrating electrons without altering their energies. Hence, the external heat generation term, S_{T}, is included only in the electron-temperature equation (see Eq. (9)). It is the electron-energy deposition distribution obtained from the Monte Carlo simulation for the electron-beam. Based on our numerical experiments, the deposition profile typically reaches steady-state (or becomes fully-developed) in less than a few femto-seconds (fs) after the beam is turned on. Since the thermal response of the target material caused by the beam lasts more than tens of nanoseconds (ns), the impact of the transient behavior of the MC profile will not be greatly evident in the simulation unless the fs regime is considered. We assume that the electron deposition profile remains constant during the TTM calculations for the sake simplicity. The effect of the transient behavior of the MC profile on the thermal response of the material will be studied in later work.

Table 1
Computational parameters used in the simulation

Property	References
$C_{\mathrm{e}} = 70T_{\mathrm{e}}$ (J/m^3 K)	[8–11]
$k_{\mathrm{e}} = C\vartheta_{\mathrm{e}}\frac{(\vartheta_{\mathrm{e}}^2+0.16)^{5/4}(\vartheta_{\mathrm{e}}^2+0.44)}{(\vartheta_{\mathrm{e}}^2+0.092)^{1/2}(\vartheta_{\mathrm{e}}^2+0.16\vartheta_{\mathrm{l}})}$;	[10]
$\vartheta_{\mathrm{e}} = T_{\mathrm{e}}/T_{\mathrm{F}}$; $\vartheta_{\mathrm{l}} = T_{\mathrm{l}}/T_{\mathrm{F}}$	
$C_{\mathrm{l}} = 8.33\times10^{3}T_{\mathrm{l}}$ (J/m^3 K)	[8–11]
$G_{\mathrm{e\text{-}ph}} = 2.1\times10^{16}$ (W/m^3 K)	[10]

The TTM is solved numerically using a finite-difference method, where first-order time and second-order space discretizations are used. The workpiece (anode) is 1 μm thick and 8.5 μm wide in both lateral directions. The properties assumed in the simulations are listed in Table 1. The workpiece is assumed to be gold under a vacuum condition of 10^{-8} torr. Hence, the two possible heat transfer mechanisms are conduction and radiation. We initially included a simple radiation-conduction model to account for emission from the workpiece; however, we did not observe any significant effect of radiation in our simulations within the small time durations we consider. Thus, we neglect radiation losses and assume adiabatic boundary conditions for all surfaces. This simplification improves the speed-up of convergence for the analysis. A more detailed study that includes radiation emission at the micro/nanoscale is required in future work after we observe the structural changes in the material due to nanoscale material removal.

The melting temperature for gold is around 1336 K [12]; however, the sublimation temperature for gold is around 1080 K for a vacuum pressure of 10^{-8} torr [13]. As a result, gold tends to sublimate before melting. Although this is the scenario, heating in the simulation will be limited to be below the sublimation temperature. The goal in this work is to determine the range of applicability of the TTM compared to Fourier’s heat conduction equation.

4. Results and discussion

4.1. Electron-energy deposition distributions

In the numerical simulations, the electron-energy deposition profiles for various cases are first computed, as discussed in Section 3.2. These results are displayed in Figs.

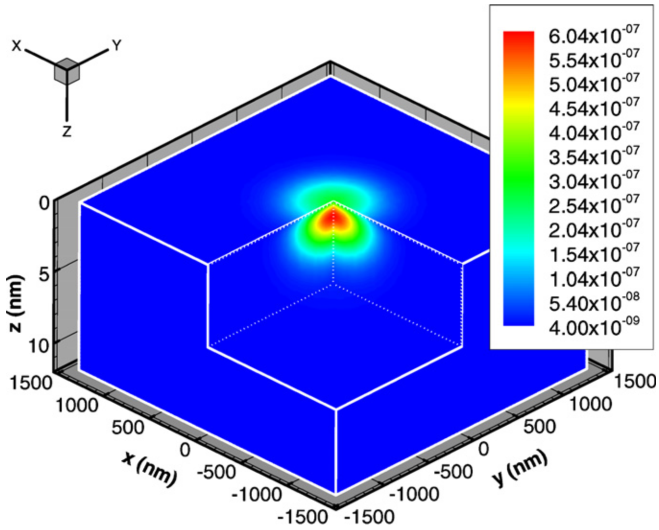

Fig. 3. Electron-energy deposition distributions for $R_{\text{beam}} = 500$ nm and $E_0 = 500$ eV is shown. The numbers given in the figure are in terms of normalized quantities, per unit nm^3.

3 and 4. A Gaussian incident beam profile for incident electrons with $1/e^2$ radius at R_{beam} is used. For the case shown in Fig. 3, the initial kinetic energy of the electron-beam is 500 eV and R_{beam} is 500 nm. Values given in the figure were normalized with respect to the total electron-energy supplied from the electron-beam and the corresponding volume of the computational element. A series of numerical experiments revealed that 20% grid stretching beyond the uniform grid is acceptable for these simulations. While it is possible to solve the problem in the cylindrical coordinate system, which would reduce the computation to two dimensions (since the electron-beam impinges normally on the workpiece), the problem is solved in three dimensions so that the implementation of an oblique and/or moving incident electron-beam can be easily considered in the future without imposing numerous modifications to the code.

In a typical electron-energy deposition distribution, the deposition amount is usually maximum at a point below the workpiece's surface, as is evident in Figs. 3 and 4. In Fig. 4, the distributions are shown in *x*–*z* plane for the ease of visualization. Two important parameters that can be adjusted in the code are the initial incident kinetic energy, E_0, and the $1/e^2$ Gaussian radius, R_{beam}, of the electron-beam. Fig. 4a shows the case where $E_0 = 500$ eV and $R_{\text{beam}} = 100$ nm, and the deposition amounts are in the order of 10^{-5} per unit nm^3. When the radius of the beam is increased (i.e. $R_{\text{beam}} = 100$–500 nm), the deposition amounts drop to the order of 10^{-7} per unit nm^3, as shown in Fig. 4b. This is expected since electrons are more widely spread when the radius of the beam broadens, which then

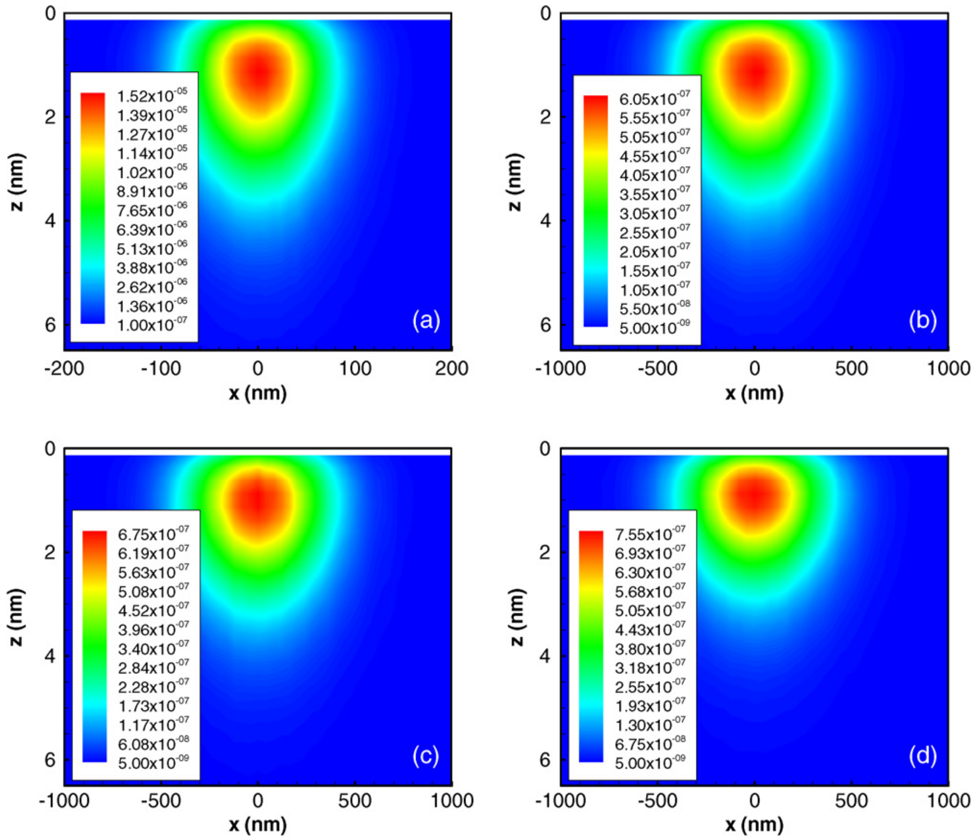

Fig. 4. Electron-energy deposition distributions for four different cases are depicted: (a) $R_{\text{beam}} = 100$ nm and $E_0 = 500$ eV, (b) $R_{\text{beam}} = 500$ nm and $E_0 = 500$ eV, (c) $R_{\text{beam}} = 500$ nm and $E_0 = 420$ eV, and (d) $R_{\text{beam}} = 500$ nm and $E_0 = 350$ eV. The numbers given in the figure are in terms of normalized quantities, per unit nm^3.

results in a wider spatial energy spread and lower deposition amounts. In Fig. 4c and d, the R_{beam} is fixed at 500 nm while E_0 is set to 350 eV and 420 eV, respectively. The deposition profiles start to shrink in the z-direction when the energy of the beam decreases. This is due to the fact that the electron penetration depth becomes shallower when the initial kinetic energy is lower. However, the maximum energy deposition amount increases as the electron-beam energy is lowered.

4.2. Thermal heating using an electron-beam

Using the electron-energy deposition distributions obtained in the previous section, the temperature increase in gold due to the incidence of an electron-beam is determined with the TTM. In order to obtain accurate temperature simulations, a number of numerical experiments are carried out. The time step is changed while holding other parameters fixed. It is found that several different values of time step are required to resolve the transient temperature profile. The transient response of the material due to the heating by the electron-beam is spread over a wide range of time. Based on the input values and heating profiles in the current work, the transient temperature profiles typically range from femto-seconds to nanoseconds. Using a uniform time step of several femto-seconds throughout the entire simulation to resolve the transient temperature profile is not practical because of the enormous number of iterations needed to reach nanosecond intervals. Therefore, a simulation case is typically run several times with different time steps to determine its complete transient temperature curve. Fig. 5 depicts the evolution of the maximum electron-temperature and phonon-temperature in the gold layer (i.e. 8.5 μm × 8.5 μm × 1 μm) as a function of time, when it is exposed to an electron-beam with specifications from Fig. 4b. Sequels of the transient electron- and phonon-temperatures are captured with four time steps ranging from 1×10^{-11} s to 1×10^{-15} s. The maximum electron-temperature, which is denoted as $T_{\text{e,max}}$, increases as time progresses when electrons inside the gold layer absorb the incoming energy provided by the electron-beam. The maximum phonon-temperature, $T_{\text{ph,max}}$, increases gradually through the electron–phonon energy coupling. We did similar investigations for the spatial steps, and dx, dy, and dz were determined to be 40 nm, 40 nm, and 0.25 nm, respectively. The reasonable grid stretching in our simulation is 20%, as mentioned previously.

Fig. 6a shows a typical temperature distribution of the workpiece as heated by the electron-beam. The figure depicts an instantaneous snapshot of the electron-temperature field at an elapsed time of 0.1 μs. The current of the electron-beam used in this case is 0.5 mA while the electron-energy deposition profile is given in Fig. 4b. The phonon-temperature is not shown here since it is identical to the electron-temperature plot, because both the electron-temperature and the phonon-temperature are converged into a single temperature by 0.1 μs.

By holding other computational parameters constant and varying the thickness of the workpiece, one can observe how the workpiece thickness affects transient temperature behavior (see Fig. 7a). The transient electron and phonon-temperature profiles for two different thicknesses are identical until about 2 ns, at which point they start to deviate from one another. This deviation time implies that the effect of the bottom boundary is not evident before 2 ns. Intuitively, one expects the material to sublimate faster for a thinner workpiece when compared to a thicker one. This is seen in Fig. 7a where the sublimation time increases as one increases the thickness of the workpiece from 500 nm to 1 μm.

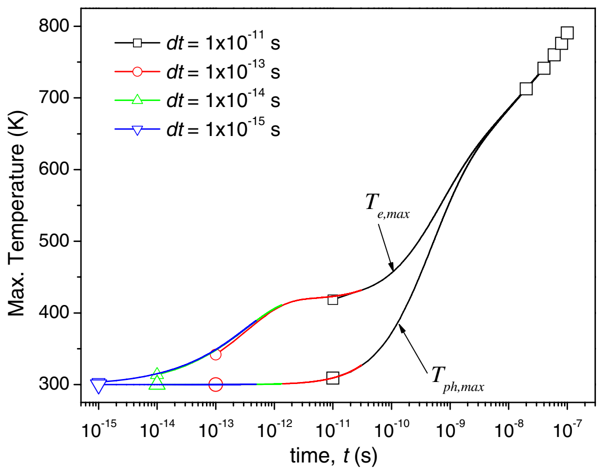

Fig. 5. The maximum transient electron- and phonon-temperature curves of the target workpiece in unit of Kelvin for the case where $R_{\text{beam}} = 500$ nm and $E_0 = 500$ eV are shown. The current of the electron-beam used is 0.5 mA.

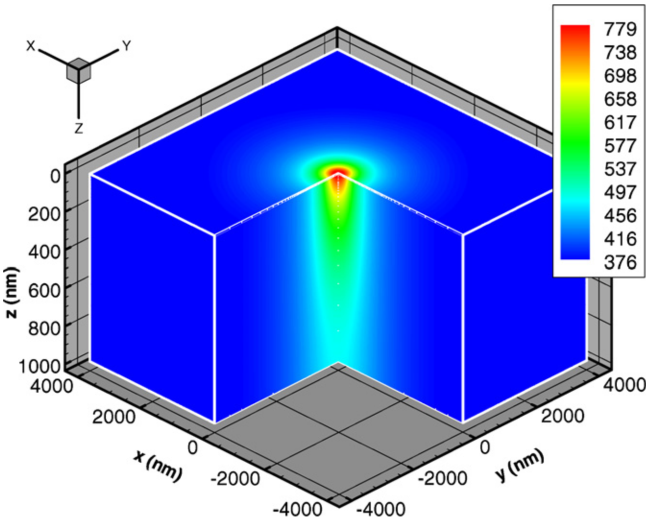

Fig. 6. The electron-temperature distribution of the target workpiece in unit of Kelvin for $R_{\text{beam}} = 500$ nm and $E_0 = 500$ eV is shown. The current of the electron-beam used is 0.5 mA, and the temperature profile shown is the snapshot at $t = 0.1$ μs.

The effect of the initial kinetic energy of the electron-beam on the transient behavior of the temperature is also examined. Two different choices of initial kinetic energy of the electron-beam, 350 eV and 500 eV, were considered. The effect of the initial kinetic energy on the transient behavior is that one can delay the sublimation in the workpiece by lowering the initial energy of the beam, as shown in Fig. 7b. Similarly, one can produce the same effect of delaying the sublimation by lowering the power of the electron-beam, which is evident in Fig. 7c.

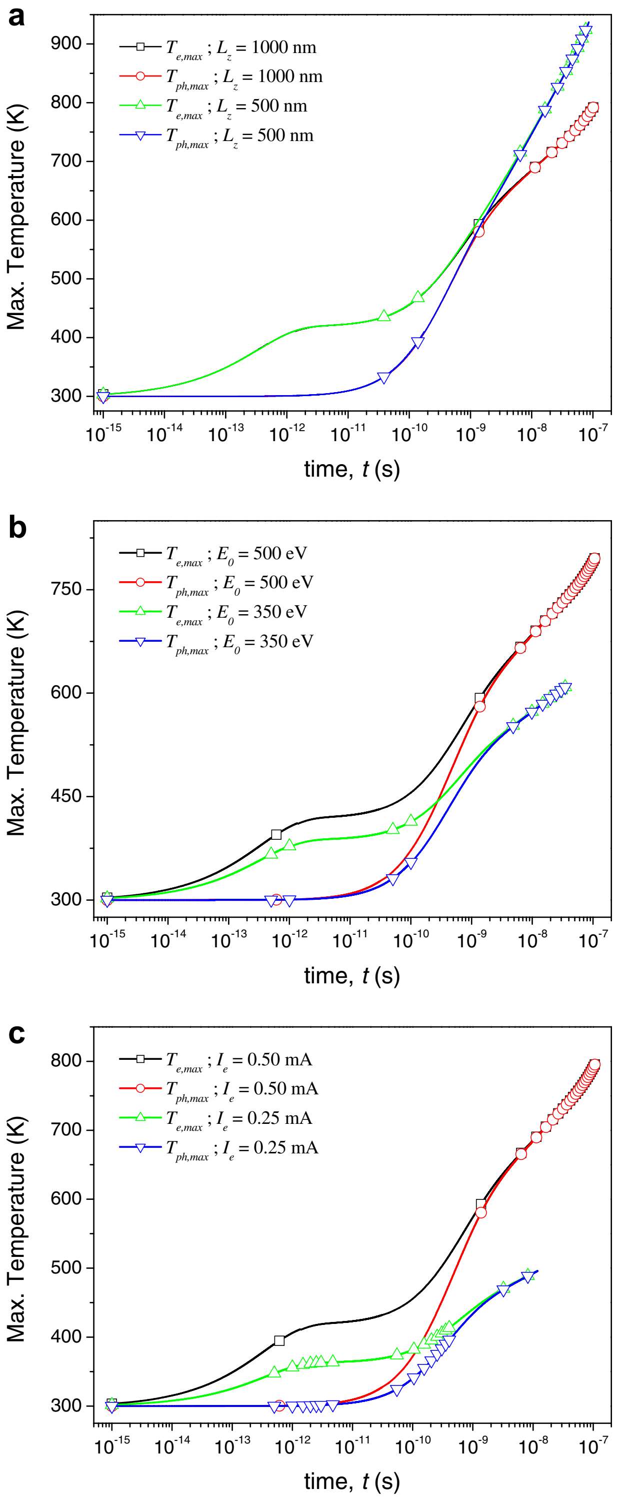

Fig. 7. The effects of, (a) workpiece thickness, (b) initial electron kinetic energy, and (c) electric current of the electron-beam, on the maximum transient electron-temperature and phonon-temperature are given.

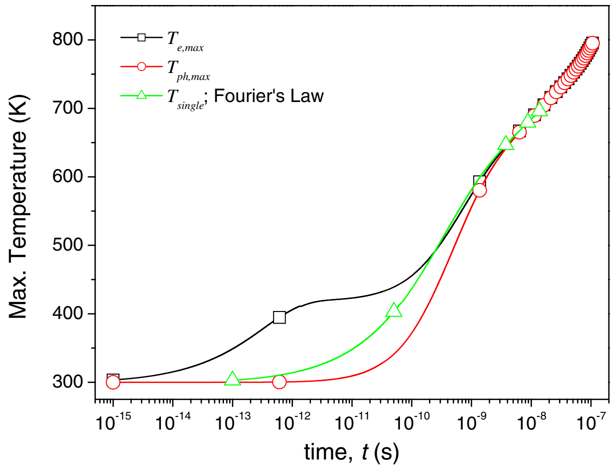

Fig. 8. The comparison between maximum temperatures predicted using the Fourier heat conduction equation and the two-temperature model is shown. The parameters used are $R_{\mathrm{beam}} = 500$ nm, $E_0 = 500$ eV, $I_e = 0.5$ mA, and $L_z = 1000$ nm.

An interesting trend, that all these transient figures demonstrate, is that both the electron-temperature and the phonon-temperature converge into a single curve when the heating time is beyond 5 ns, suggesting that the Fourier heat conduction equation is applicable. To verify this, the Fourier heat conduction equation is used to simulate a test case where $R_{\mathrm{beam}} = 500$ nm, $E_0 = 500$ eV, $I_e = 0.5$ mA, and $L_z = 1000$ nm. The simulation result predicted using this approach is plotted against that of the TTM, which is shown in Fig. 8. It is clear from Fig. 8 that both the Fourier heat conduction equation and the TTM yield the same temperature profile after an elapsed time of 5 ns. In the simulations, the electron-beam starts heating the workpiece at time "zero," and within the first 5 ns, the electron-temperature always exceeds phonon-temperature. This difference could not have been identified with the Fourier model (FM). If there is no need to discern the profile within the first few nanoseconds, the simpler FM is adequate.

5. Conclusions

A detailed model is presented to simulate heat transfer induced by an electron-beam from a nanoscale probe. The propagation of electrons in the workpiece and their interaction with the lattice is considered separately by coupling the discrete inelastic scattering Monte Carlo approach for the electron-beam with a two-temperature model for the electron–phonon equation. It is observed that a 500-eV electron-beam with a $1/e^2$ Gaussian radius of 500 nm and a current of 10 mA is capable of sublimating gold under a vacuum pressure of 10^{-8} torr. The dimensions of the gold workpiece were chosen as 1 μm × 8.5 μm ×

8.5 μm. to accommodate the available computational resources. A parametric study is outlined for understanding the effects of these parameters on the transient behavior of the temperature profile in the workpiece.

The numerical experiments reveal that for time-durations longer than approximately 5 ns, temperatures of the electrons and phonons in the gold layer always reach equilibrium. This implies that the Fourier law of heat conduction is acceptable for machining times beyond a few nanoseconds, for the specific set of parameters used here. Using the presented methodology, additional numerical experiments can be enacted as there are many different nanoscale machining scenarios for many computational parameters. Additional results from other simulations using this method are described by Wong [14]. We are in the process of replacing the two-temperature model with the hydrodynamic electron–phonon equations, where the electron continuity and momentum equations are included in the computations. As a result, the electrical flow in the workpiece can also be analyzed. Further details of this approach are also discussed by Wong [14], and they will be reported in a future publication.

Acknowledgement

This work is supported by an NSF Nanoscale Interdisciplinary Research Team (NIRT) award from the Nano-Manufacturing program in Design, Manufacturing, and Industrial Innovation (DMI-0210559).

References

[1] R.R. Vallance, A.M. Rao, M.P. Mengüç, Processes for Nanomachining Using Carbon Nanotubes, University of Kentucky Research Foundation, U.S.A., 2003, Patent No. 6,660,959.

[2] B.T. Wong, M.P. Mengüç, R.R. Vallance, Nano-scale machining via electron beam and laser processing, ASME J. Heat Transfer 126 (4) (2004) 566–576.

[3] D.C. Joy, Monte Carlo Modeling for Electron Microscopy and Microanalysis, Oxford University Press, New York, 1995.

[4] B.T. Wong, M.P. Mengüç, R.R. Vallance, Sequential nano-patterning using electron and laser beams: a numerical methodology, J. Comput. Theor. Nanosci. 3 (2) (2006) 1–12.

[5] M. Dapor, Electron-Beam Interactions with Solids, Springer-Verlag Berlin Heidelberg, Berlin, 2003.

[6] Z.J. Ding, R. Shimizu, A Monte Carlo modeling of electron interaction with solids including cascade secondary electron production, Scanning 18 (1996) 92–113.

[7] B.T. Wong, M.P. Mengüç, Monte Carlo methods in radiative transfer and electron-beam processing, J. Quantitat. Spectros. Radiat. Transfer 84 (2004) 437–450.

[8] D.Y. Tzou, Macro- to Microscale Heat Transfer, Taylor & Francis, Washington, DC, 1997.

[9] N.W. Ashcroft, N.D. Mermin, Solid State Physics, Saunders Company, Philadelphia, 1976.

[10] D.S. Ivanov, L.V. Zhigilei, Combined atomistic-continuum modeling of short-pulse laser melting and disintegration of metal films, Phys. Rev. B 68 (2003) 064114.

[11] J.M. Ziman, Principles of the Theory of Solids, Cambridge University Press, Cambridge, 1964.

[12] F.P. Incropera, D.P. DeWitt, Fundamentals of Heat and Mass Transfer, fourth ed., John Wiley & Sons, New York, 1996.

[13] R.E. Honig, Vapor pressure data for the solid and liquid elements, RCA Rev. (1962) 567–586.

[14] B.T. Wong, Thermal Heat Transport at the Nano-Scale Level and Its Application to Nano-Machining, Ph.D. Thesis, University of Kentucky, Lexington, Kentucky, 2006.

[15] N.F. Mott, H.S.W. Massey, The Theory of Atomic Collisions, Oxford Clarendon Press, 1965.

[16] J. Kessler, Polarized Electrons, Springer Verlag, New York, 1976.

[17] Z. Czyzewski, D.O.N. MacCalium, A. Romig, D.C. Joy, Calculations of Mott scattering cross section, J. Appl. Phys. 68 (7) (1990) 3066–3072.